Supporting Information for:

Galvanic Replacement of Intermetallic Nanocrystals as a Route Toward Complex Heterostructures

Alexander N. Chen, Emma J. Endres, Hannah M. Ashberry, Sandra L. A. Bueno, Yifan Chen, and Sara E. Skrabalak*

Department of Chemistry, Indiana University - Bloomington, Bloomington, Indiana 47405, United States

Table of Contents

Experimental

Chemicals. Oleylamine (OlAm, 70%), oleic acid (OA, 90%), trioctylphosphine (TOP, 97%), copper (II) acetylacetonate ($Cu(acac)_2$, 97%), copper (II) acetate ($Cu(ac)_2$, 98%), palladium (II) chloride ($PdCl_2$, 99.9%), palladium (II) bromide ($PdBr_2$, 99%), cetyltrimethylammonium bromide (CTAB, 99%, lot #s BCBT1510, BCBW9460), chloroauric acid ($HAuCl_4 \bullet 3H_2O$, 99.9%), and hydrogen hexachloroplatinate hexahydrate ($H_2PtCl_6 \bullet 6H_2O$, 99.98%) were purchased from Sigma-Aldrich. Ethanol (200 proof, anhydrous, 99.5%) was purchased from Pharmco. Acetone (99.5%) was purchased from Macron. Hexanes (ACS reagent) were purchased from J. T. Baker. Nanopure water (18.2 MΩ•cm) was used in all phase transfer and galvanic replacement experiments.

Synthesis of B2 PdCu templates. Intermetallic PdCu B2 templates were synthesized based on a modified literature protocol.[1] 36 mg $Cu(ac)_2$ and 54 mg $PdBr_2$ were dissolved in a magnetically stirred solution of 18 mL OlAm and 120 µL OA under vacuum at 100 °C for 10 min, after which 30 µL TOP was added. The solution was heated to 235 °C under Ar, and held there for 30-35 min, before being cooled naturally to 50-70 °C. The reaction solution was centrifuged at 3900 RPM for 10 min to collect the particles and then the obtained particles were washed 3 times with a mixture of ethanol and hexane (5:1 vol). The particles were suspended in hexane for further use.

Synthesis of A1 PdCu templates. The alloy PdCu A1 NPs were obtained based on a modified protocol previously reported.[2] $PdCl_2$ (0.1 mmol), $Cu(acac)_2$ (0.1 mmol), and 5 mL of oleylamine was added to a 50 ml three-neck round-bottom flask and was heated under Ar while stirring for 30 minutes at 100 °C. Then the reaction solution

was heated to 235 °C under Ar and hold at that temperature for 30 minutes. The solution was allowed to cool to room temperature and centrifuged at 3900 RPM for 10 minutes to remove the larger particles. Then, the rest of the particles were precipitated out by acetone and collected by centrifugation. The particles were then suspended in 4 mL of hexane.

Phase transfer. B2 and A1 PdCu templates were transferred from hexane to aqueous solution following a modified literature protocol.[3] 250 μL of hexane-suspended PdCu nanoparticles were added to an 8-dram vial. The hexane was evaporated under air. Particles were resuspended in 500 μL OlAm by mixing and brief sonication. To the OlAm suspension was added 20 mL of a 25 mM CTAB solution where the solvent was a 1:2 EtOH:H_2O mixture. The capped vial was inverted several times, until the solution appeared homogeneous. The amount of the hexane suspension used in the beginning could be decreased if the solution did not turn homogeneous, or if particles started sedimenting out. This solution was centrifuged for 10 min at 15 000 RPM, and the pellet resuspended in 500 μL H_2O. To keep constant particle concentrations across experiments, many phase transfers can be done in parallel, and combined at this point. To remove ethanol, the resulting solution was heated at ~70 °C under air for ~1 h.

Galvanic replacement. Galvanic replacement experiments were based on a literature procedure.[4] Typically, solutions of 0.1 mM $HAuCl_4$ or 0.2 mM H_2PtCl_6 were injected using a syringe pump, usually at a rate of 0.25 mL/min, into refluxing solutions composed of 5 mL 4.5 mM CTAB and 500 μL of seeds, inside a round bottom flask. Solutions were kept refluxing by being suspended in an oil bath set to 115 °C. Reaction

solutions were stirred at 300 RPM using egg-shaped stir bars (VWR catalog # 58949-010). 10 min (for $HAuCl_4$) or 30 min (for H_2PtCl_6) after the oxidant solution was finished being injected, reaction solutions were removed from the oil bath to cool down. Products were then collected by centrifuging for 20 min at 8000 RPM, and then redispersed in 600 μL H_2O.

Galvanic replacement – additional notes. Phase transfer procedures do not always result in aqueous solutions with the same concentration. Relative concentrations could be determined by performing a typical galvanic replacement reaction with B2 templates and $HAuCl_4$, and matching the resulting compositions and morphologies to Figures 1 and 3. From there, the standard 500 μL of seeds to use in subsequent galvanic replacement reactions can be changed to account for different concentrations. To obtain products in the row marked "All at once" in Figure S8, the entire listed volume of 0.1 mM $HAuCl_4$ solutions were injected all at once using a pipette into a typical refluxing solution of intermetallic templates. To obtain products such as those shown in Figure S9, 720 μL 10 mM $HAuCl_4$ were injected all at once using a pipette into a typical refluxing solution of intermetallic templates.

Characterization. Transmission electron microscopy (TEM) images were taken using a JEOL JEM 1010 TEM operated at 80 kV with a spot size of 1, and a JEOL JEM 3200FS TEM operated at 300 kV with a spot size of 1. STEM images and corresponding energy-dispersive X-ray spectroscopy (EDS) elemental mapping were obtained using an Oxford Aztec energy dispersive X-ray detector interfaced to the JEOL JEM 3200FS operating in STEM mode. High-resolution STEM imaging and accompanying elemental mapping were obtained using a Thermo Scientific Themis Z

advanced probe aberration-corrected analytical TEM/STEM with FEI super-X EDS detection system operated at 300 kV. TEM samples were prepared by drop-casting dispersed aqueous particle solutions onto carbon-coated Ni grids (or Cu grids, if STEM-EDS was not needed), and rinsing grids with acetone before the aqueous sample could dry. Bulk-scale elemental compositions were determined using an Oxford Aztec energy dispersive X-ray detector interfaced to a FEI Quanta 600F environmental scanning electron microscope (SEM) operated at 30 kV with a spot size of 3. SEM-EDS samples were prepared by drop-casting aqueous particle solutions onto Si wafers, allowing the aqueous sample to dry, and then rinsing the Si wafer with methanol. Powder X-ray diffraction patterns were obtained on a PANalytical Empyrean X-ray diffractometer using Cu Kα radiation (λ = 0.15418 nm). X-ray photoelectron spectroscopy (XPS) measurements were performed using a PHI 5000 Versa Probe II scanning X-ray microprobe operated under ultrahigh vacuum conditions and using a monochromatic Al Kα X-ray source. All spectra were referenced to the C 1s peak at 284.8 eV.

Discussion of B2 replacement product polydispersity. To obtain a representative measurement for each sample in bulk SEM-EDS, EDS scans were performed on densely-packed areas spanning multiple square microns, and at eight different locations separated from each other by tens of microns. Given the observation of shape and composition polydispersity in the intermediate stage (Figure S3), it is possible that the outliers in Figure 3 may be due to micron-scale particle segregation. Indeed, some particle segregation can be seen at this stage in high-magnification STEM-EDS, where Figure S8 shows elemental compositions determined by EDS of four points in the same sample as for Figure 1B and Figure S3. Notably, three of these points possess particles with multiple phases seen by *z*-contrast, and are ~40% Au with Cu:Pd ratios between 0.56-0.67, while one, Figure S8B, possesses particles with one visible phase and are ~4% Au with a Cu:Pd ratio of 0.56. So, if different types of particles also segregate by shape or composition over long distances during SEM-EDS sample preparation, it is possible that sample polydispersity may be responsible for inconsistencies in the behavior of the Cu:Pd ratio in the intermediate stage of Figure 3. In addition, this evidence of at least intermediate-stage polydispersity indicates significant differences in Au growth between particles. The PdCu templates should all have been oxidized to some extent, as the low Cu:Pd ratios at all sites suggest, but only three of four sites in Figure S8 experienced Au growth: nucleation and growth of Au seems to be separate from Cu oxidation. The separation can be associated with Cu^+ intermediates as discussed in the main text.

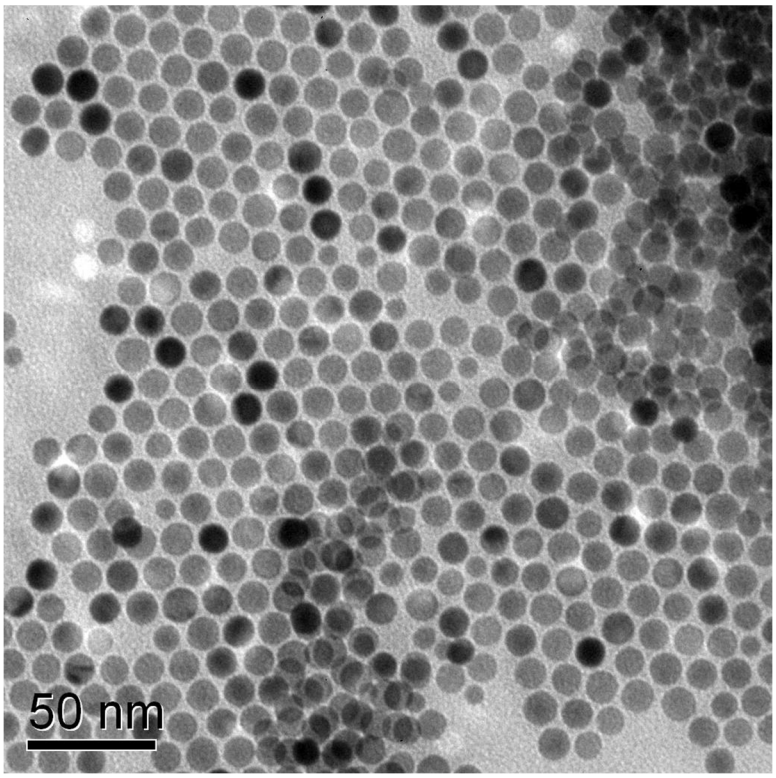

Figure S1. TEM image of PdCu B2 seeds.

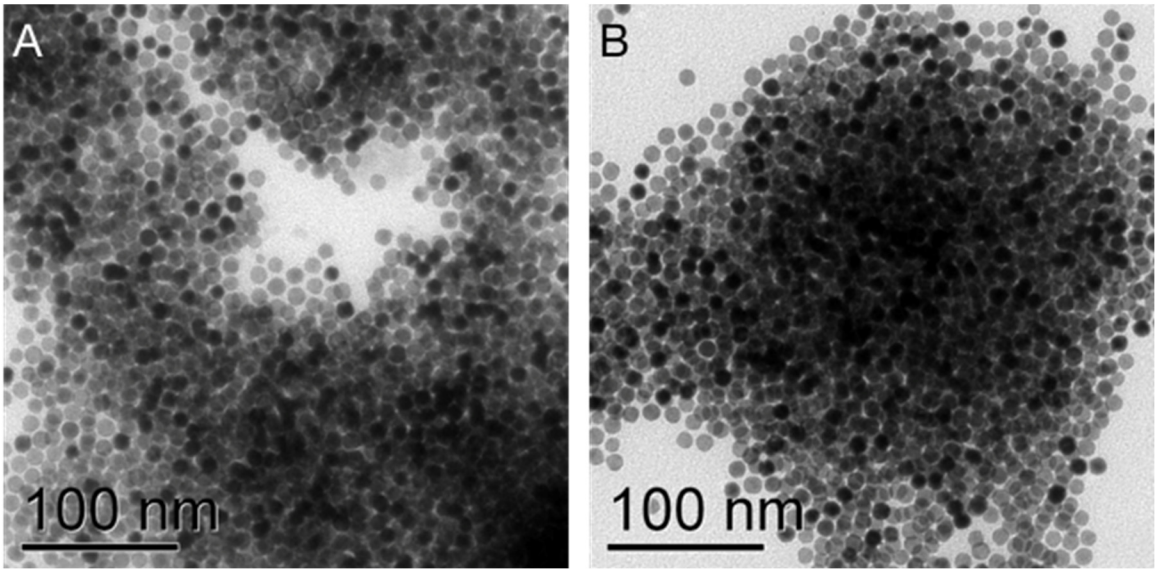

Figure S2. Low-magnification TEM images of galvanic replacement products obtained from adding 6 mL 0.1 mM $HAuCl_4$ to intermetallic PdCu templates, labeled A-B for different spots on the TEM grid for convenience.

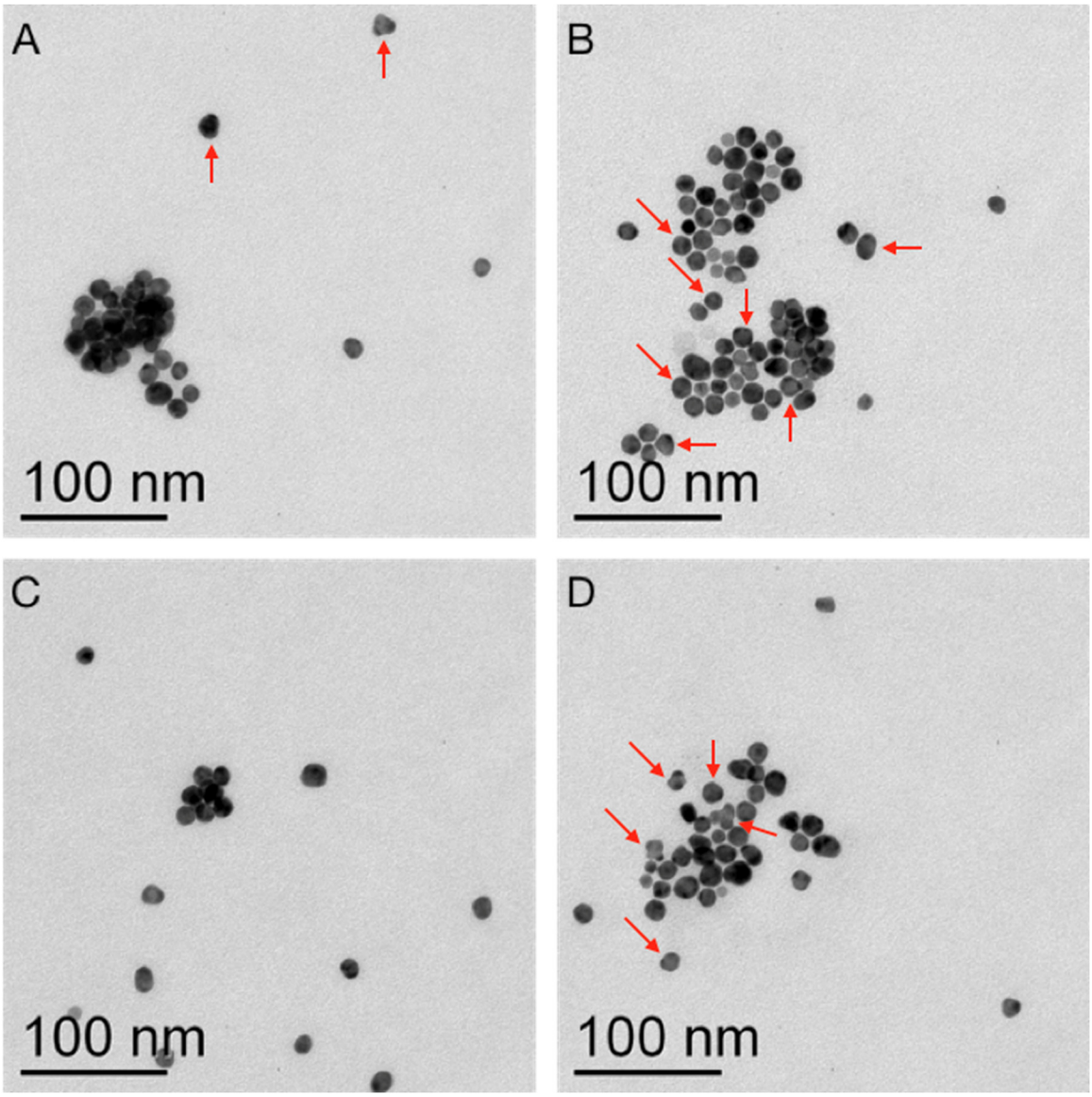

Figure S3. Low-magnification TEM images of galvanic replacement products obtained from adding 9 mL 0.1 mM $HAuCl_4$ to intermetallic PdCu templates, labeled A-D for different spots on the TEM grid for convenience. Red arrows denote examples of spheroidal particles with multiple growth points at the surface, to show that the morphology examined in Figure 1B is a common intermediate.

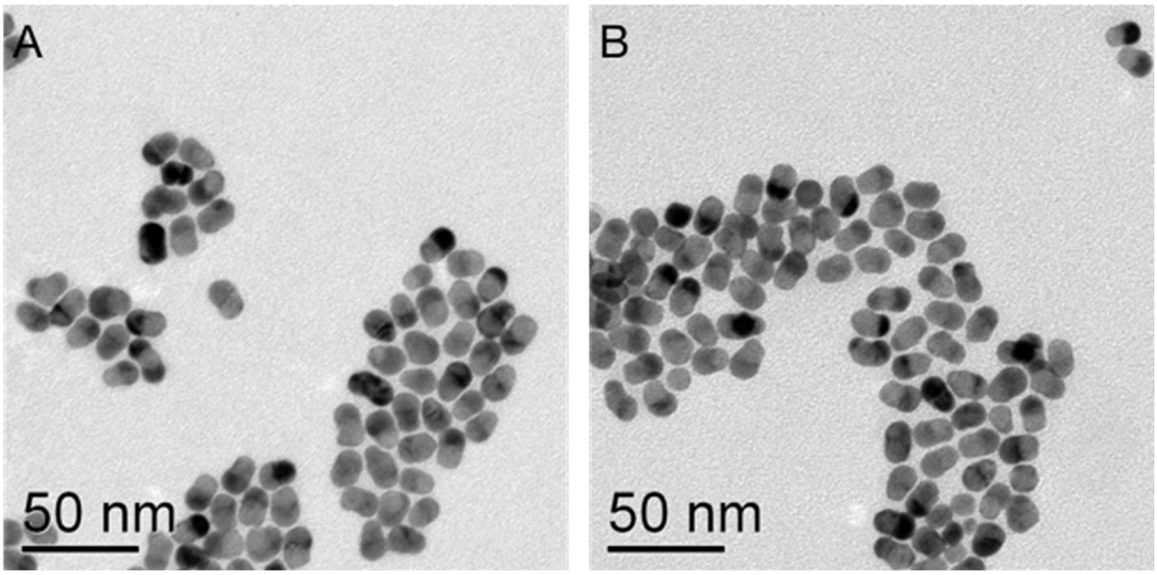

Figure S4. Low-magnification TEM images of galvanic replacement products obtained from adding 15 mL 0.1 mM $HAuCl_4$ to intermetallic PdCu templates, labeled A-B for different spots on the TEM grid for convenience.

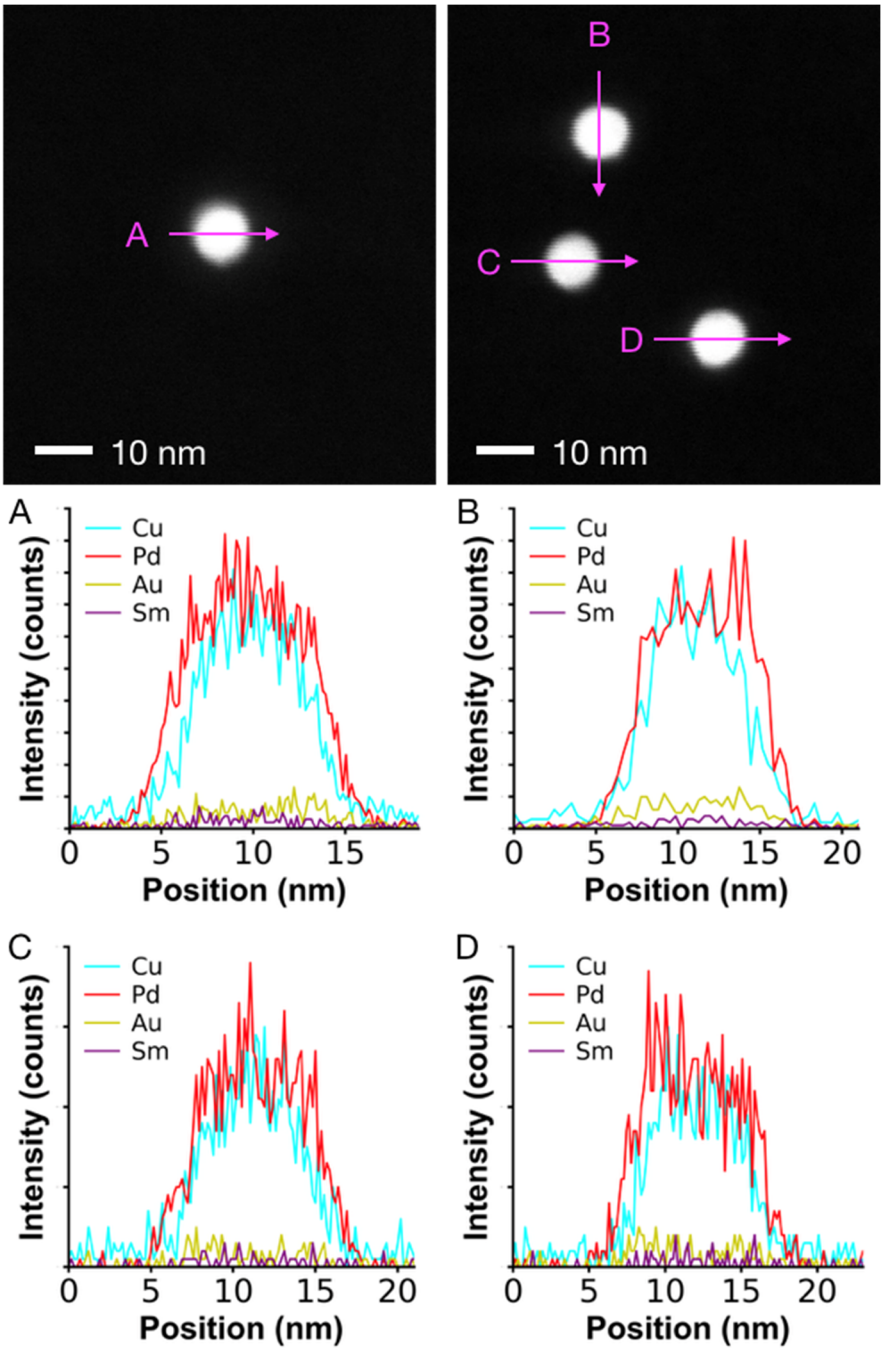

Figure S5. STEM images of the product seen in Figure 1A, including the particle that was mapped in Figure 1A on the left, along with line scans indicated by the magenta arrows and labeled A-D for convenience. Sm was chosen to represent the background signal, but was not detected in any sample. Au was automatically detected.

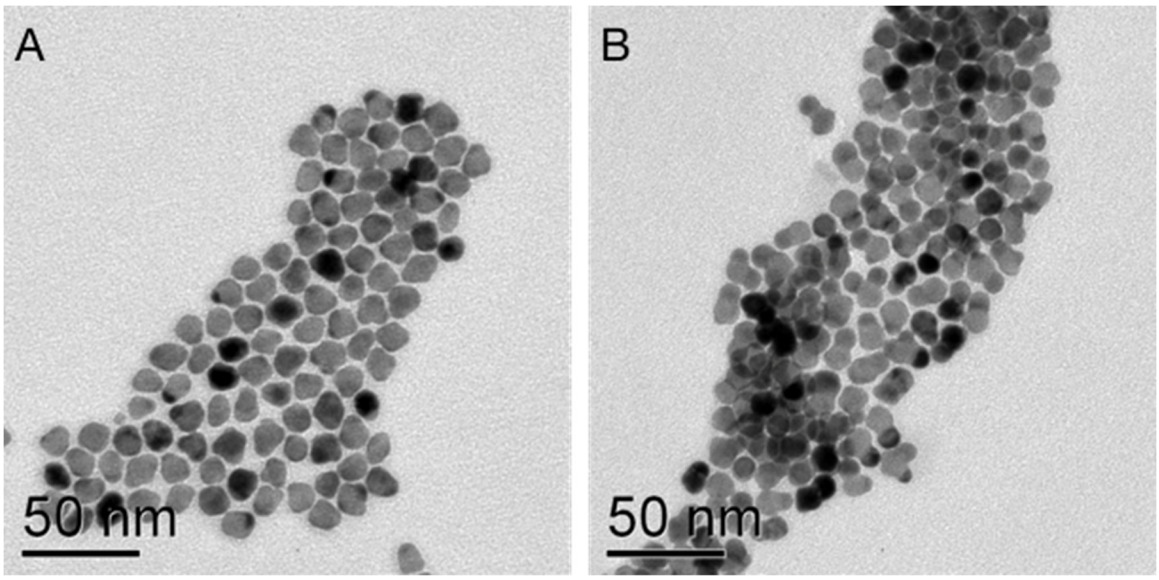

Figure S6. Low-magnification TEM images of galvanic replacement products obtained from adding (A) 7.5 mL and (B) 10 mL 0.1 mM $HAuCl_4$ to intermetallic PdCu templates.

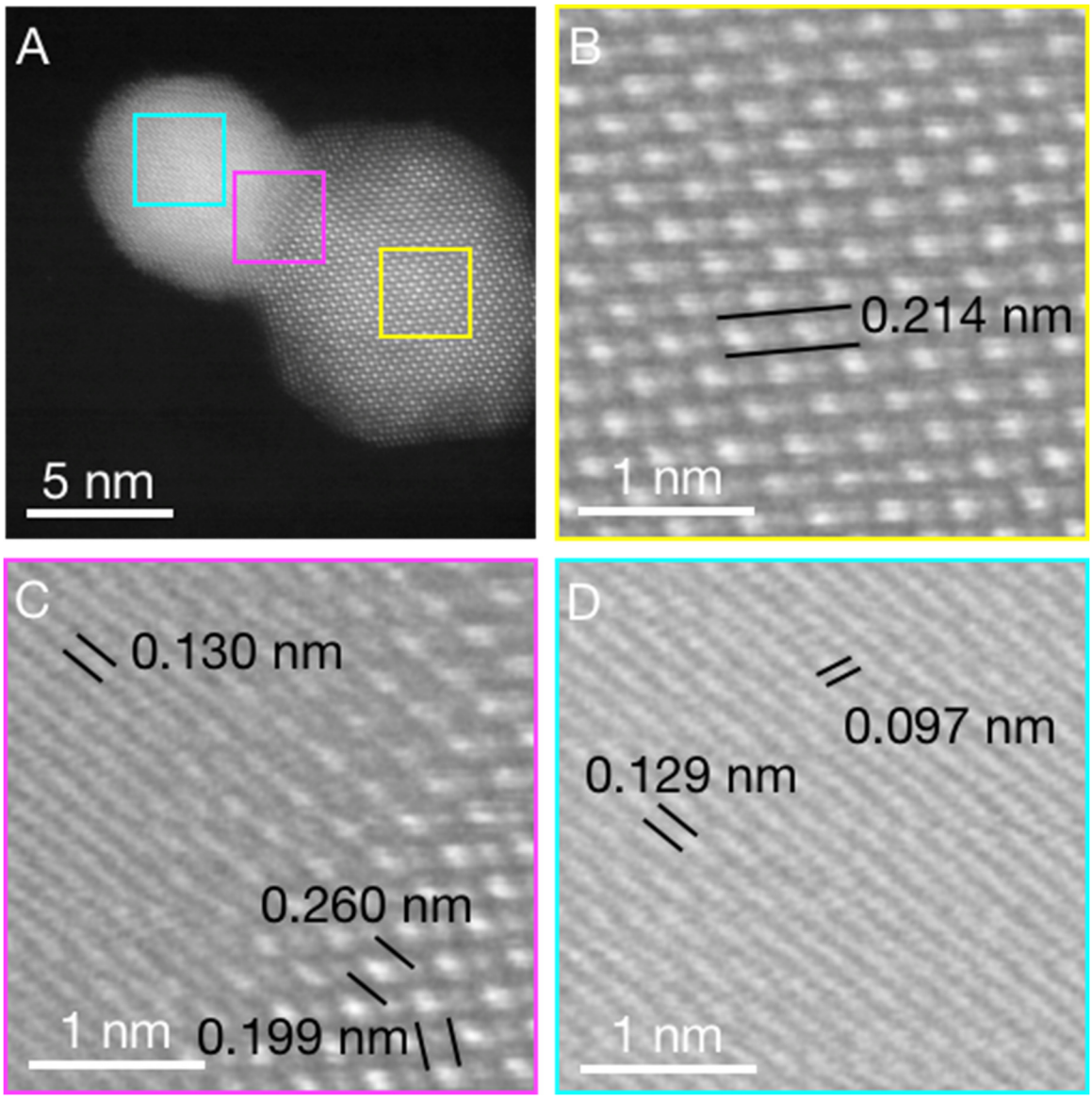

Figure S7. (A) Zoomed-out STEM image of the same particle from Figure 2A with boxes indicating three points of interest: (B) the PdCu phase, (C) the PdCu-Au interface and (D) the Au phase as Fourier-filtered images with measured lattice spacings.

Discussion of B2 PdCu-Au lattice mismatch. The calculated 3.7% lattice mismatch mentioned in the main text assumes an interface between B2 PdCu{100} and FCC Au{111} or Au {110}. The theoretical lattice spacing of B2 PdCu{100} is 0.299 nm and that for {110} is 0.211 nm.[1] The PdCu{100} plane is easily identified in Figure S5B by

the superlattice with approximately square symmetry, and further confirmed by lattice spacing measurements of 0.214 nm along the ⟨110⟩ direction. The orientation of the Au phase is more ambiguous. Using a lattice constant of 0.40782 nm,[5] the calculated lattice spacings should be 0.288 nm for Au{111} or 0.288 nm and 0.40782 nm for {110}. Counting the 2-D projections of neighboring planes such as the {220} as seen in STEM, we could also expect apparent lattice spacings of 0.144 nm for Au{110} or 0.083 nm for Au{111}. When looking at lattice spacings in the middle of the Au phase (Figure S5D), we measure 0.129 nm perpendicular to the PdCu-Au interface, which fits most closely with the shorter spacing in a {110} plane. However, the shorter spacing measures 0.097 nm, which fits most closely with Au{111}. Marginally different spacings are measured near the PdCu-Au interface in Figure S5C, where we also note the 0.260 nm {100} spacing of B2 PdCu. Importantly, the latter translates into a 0.130 nm {200} spacing, which is very close to the measured lattice spacings of the Au phase perpendicular to the interface, suggesting that the PdCu phase may be exerting a large amount of strain even many layers into the Au phase. It is therefore plausible that there is a B2 PdCu{100}-Au{111} interface wherein the Au lattice is severely distorted perpendicularly to the interface. Close observation of Figure S5D also shows irregularities in the Au lattice that may correspond to dislocations. Defects in the Au phase may be caused by strain, or hint at larger Au phases forming through coalescence of multiple smaller Au phases on the B2 surface such as those in Figure 1B, rather than through a dissolution-mediated process like Ostwald ripening.

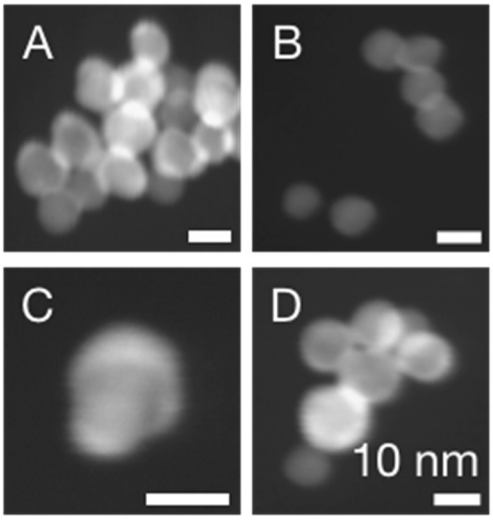

Site	Cu at %	Pd at %	Au at %
A	23.50	36.95	39.55
B	34.49	61.10	4.42
C	22.87	34.21	42.92
D	21.14	37.30	41.56

Figure S8. Left: STEM images of multiple sites, labeled A-D, in a single galvanic replacement sample resulting from adding 9 mL $HAuCl_4$ to B2 templates, also seen in Figure 1B and Figure S3. Right: elemental compositions of particles in the sites shown to the left, as determined by STEM-EDS.

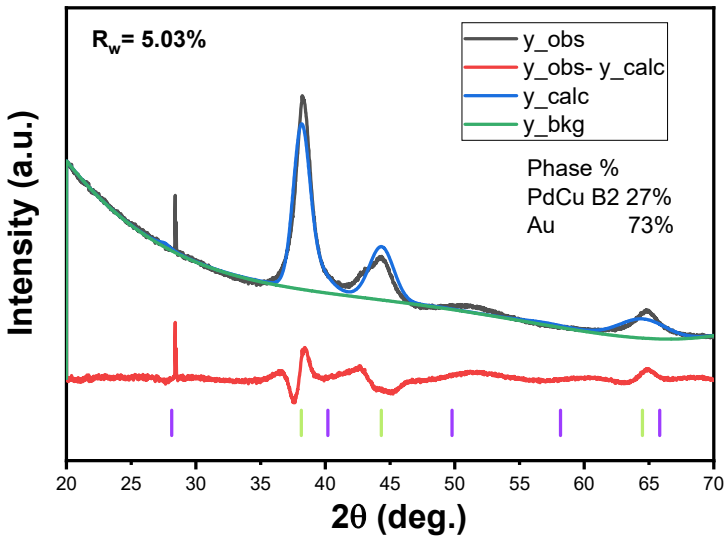

Figure S9. Rietveld refinement of the XRD pattern labeled "30 mL" from Figure 4, wherein intermetallic PdCu templates were galvanically replaced by 30 mL 0.1 mM $HAuCl_4$. Rietveld refinements of the powder diffraction data of the labeled "30 mL" from Figure 4 were performed with GSAS-II software.[6] The background was described by a Chebyshevpolynomial function and the peaks were described by the Pseudo-Voigt profile function. The scale factor, cell parameters, profile parameters (W, U, V and shape), and background points were generally refined.

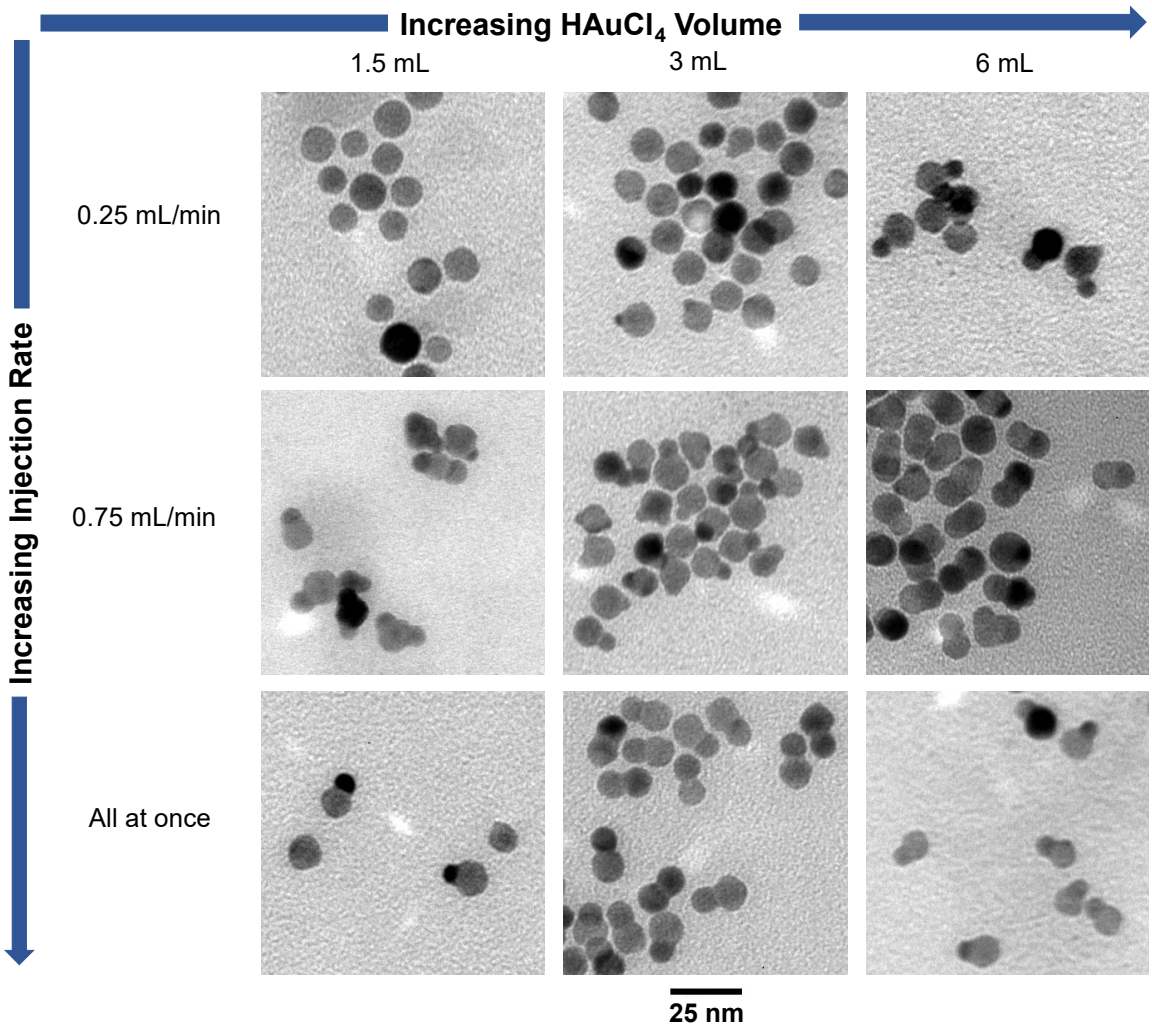

Figure S10. TEM images of galvanic replacement products obtained from injecting different amounts of 0.1 mM $HAuCl_4$ at different injection rates to intermetallic PdCu templates.

Discussion of effects of injection rate and injection volume. When 1.5 mL of precursor were added at the default rate of 0.25 mL/min, the products are spheroidal without obviously displaying new phases when imaged by TEM, but exhibit a clear change in size polydispersity compared to the B2 seeds. When the rate of injection is increased to 0.75 mL/min, one to two obviously different new phases, as seen by their different *z*-contrasts, grow on the spheroidal particles, and when the rate is increased again to injecting the precursor solution all at once, there is only one obvious point of growth

on the particles. Paralleling the increase in injection rate, increasing the injected volume at a constant 0.25 mL/min injection rate saw a progression from spheroidal products at 1.5 mL to heterodimers with very little visible overgrowth at 3 mL and clearly visible Au lobes at 6 mL. Further emphasizing the diagonal trend, adding 3 mL all at once or 6 mL at 0.75 mL/min in Figure S10 produced heterodimers with lobes of approximately equal sizes, similarly to adding 15 mL at 0.25 mL/min in Figure 1C. This trend was attributed to the fact that injected solutions were at room temperature while the reaction solution was refluxing. These synthetic conditions recall hot injection syntheses where injection of precursors causes burst nucleation while the accompanying temperature drop prevents drawn-out nucleation.[7] Brief temperature changes here can similarly produce significant changes in monomer solubility, and therefore supersaturation, mimicking the effect of increasing supersaturation by adding far more precursor without a large temperature change. The emphasis placed on burst nucleation here agrees with the nucleation event hinted at in the discussion of Figure S8.

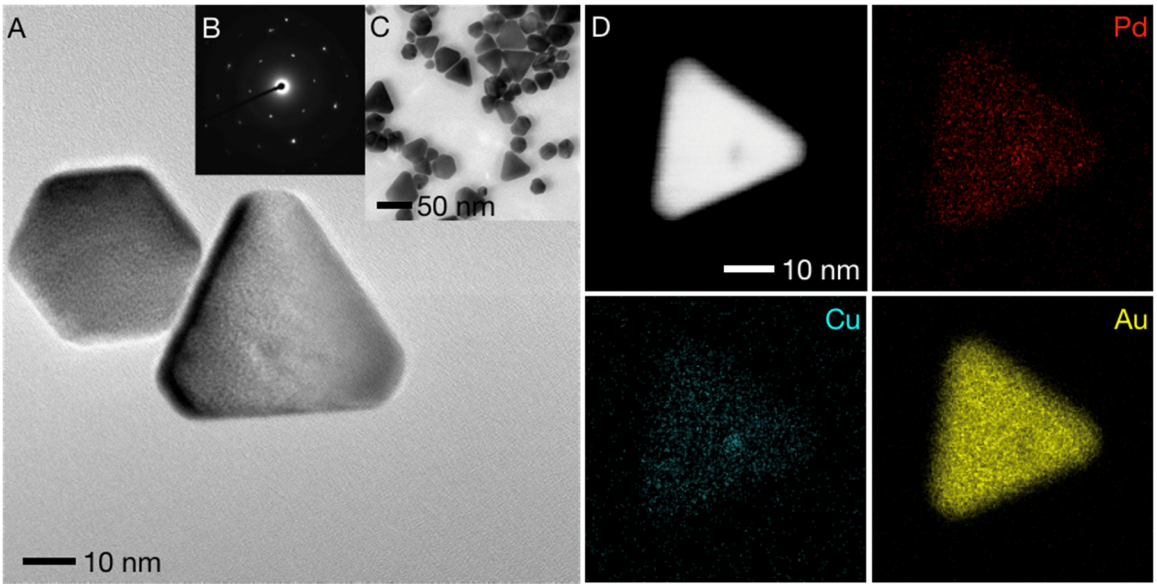

Figure S11. (A) High-magnification TEM image of plates obtained from injecting 720 μL 10 mM $HAuCl_4$ to intermetallic PdCu templates, (B) associated electron diffraction pattern confirming that these plates are {111}-faceted, (C) low-magnification TEM image of the sample, showing many plates as well as other particles with planar defects, and (D) STEM-EDS elemental map of a plate from the same sample. Cyan, Cu; red, Pd; yellow, Au.

Discussion of planar defect-rich products. We added a low volume of concentrated precursor to B2 PdCu templates all at once (720 μL 10 mM $HAuCl_4$). This reaction formed large {111}-terminated plates and other structures with planar defects like decahedra and rods, composed mostly of Au, but sometimes with a very small PdCu phase visible inside. Plates are known to possess stacking faults, implying that an extremely fast rate of galvanic replacement was capable of generating planar defects as FCC Au grew on intermetallic PdCu templates.[8] Many plates shown in Figure S11C are much larger than 10 nm in edge length, which, when compared with the 9.9 nm diameter of the original PdCu templates (Figure S1), indicates that the Au forming a single plate was likely reduced by the Pd and Cu of multiple particles, with only one PdCu seed serving as the site for Au growth.

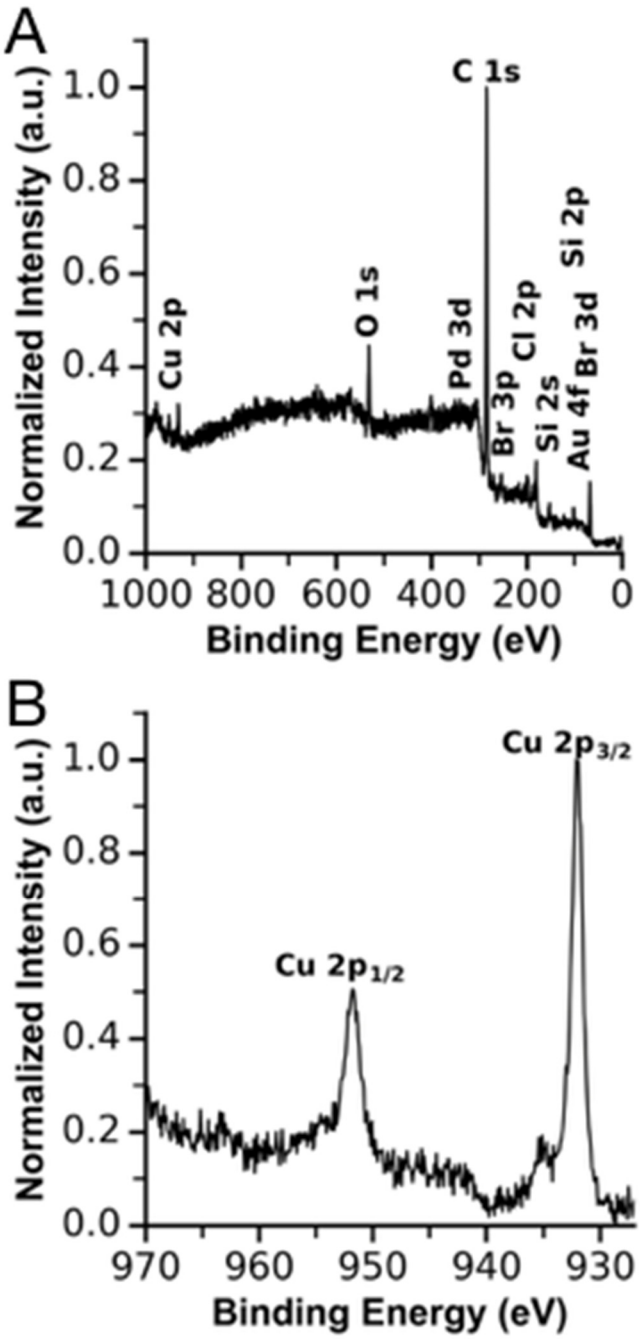

Figure S12. X-ray photoelectron spectra of the supernatant retrieved after centrifuging a galvanic replacement reaction solution in which 3 mL 0.1 mM $HAuCl_4$ were added to intermetallic PdCu templates, showing (A) survey scan and (B) high-resolution scan of Cu 2p region.

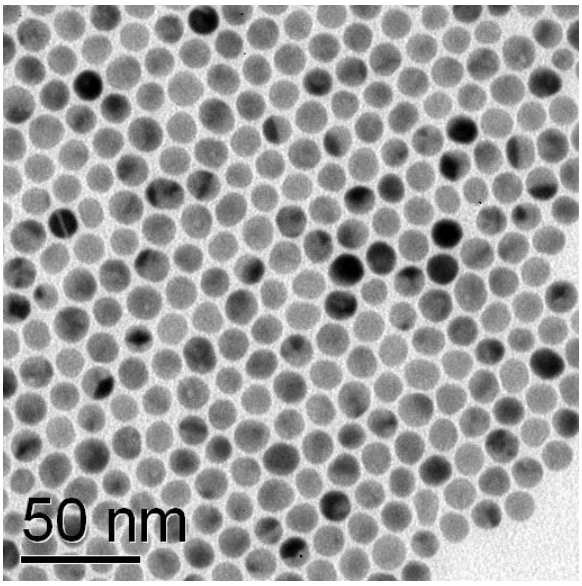

Figure S13. TEM image of A1 PdCu seeds.

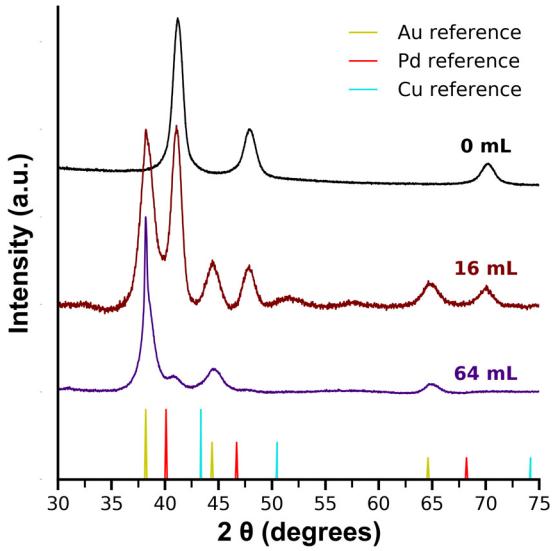

Figure S14. Background-subtracted XRD patterns corresponding to products obtained when random alloy PdCu templates are galvanically replaced by various volumes of 0.1 mM $HAuCl_4$.

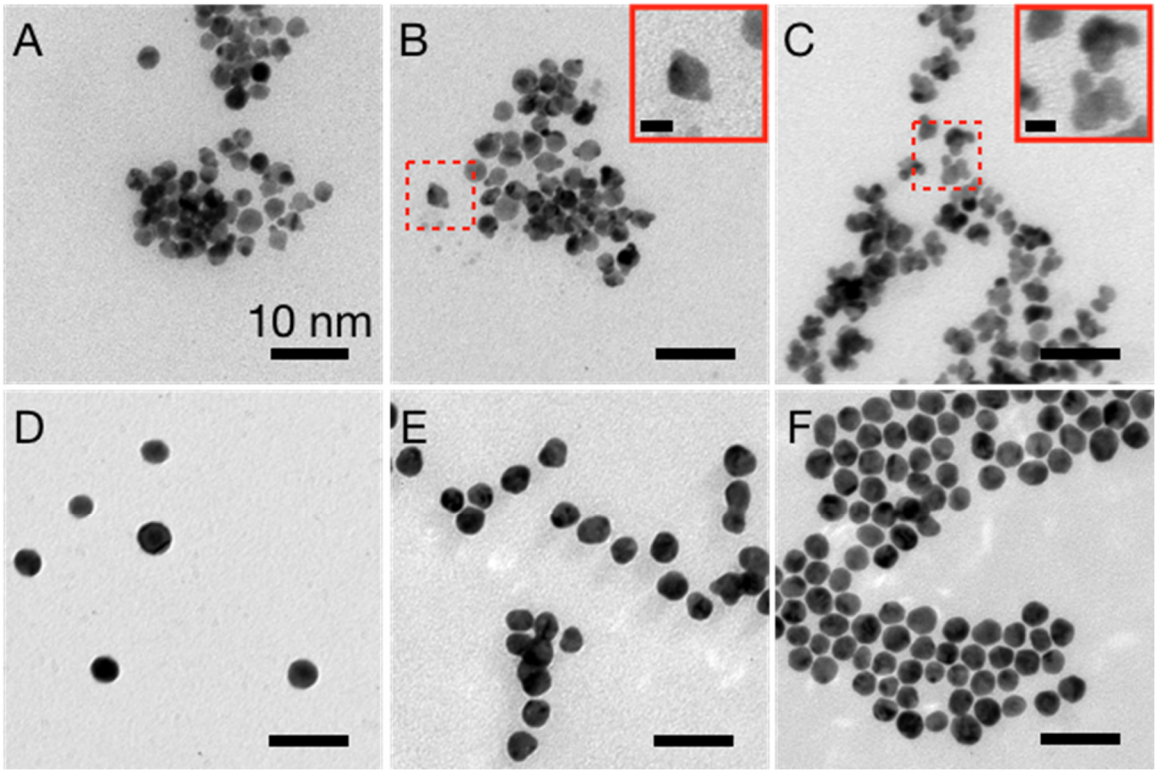

Figure S15. Low-magnification TEM images of galvanic replacement products obtained from adding (A) 2, (B) 4, (C) 8, (D) 16, (E) 32 and (F) 48 mL 0.1 mM $HAuCl_4$ to random alloy PdCu templates. Insets in panels B-C zoom in around particles with multiple points of overgrowth.

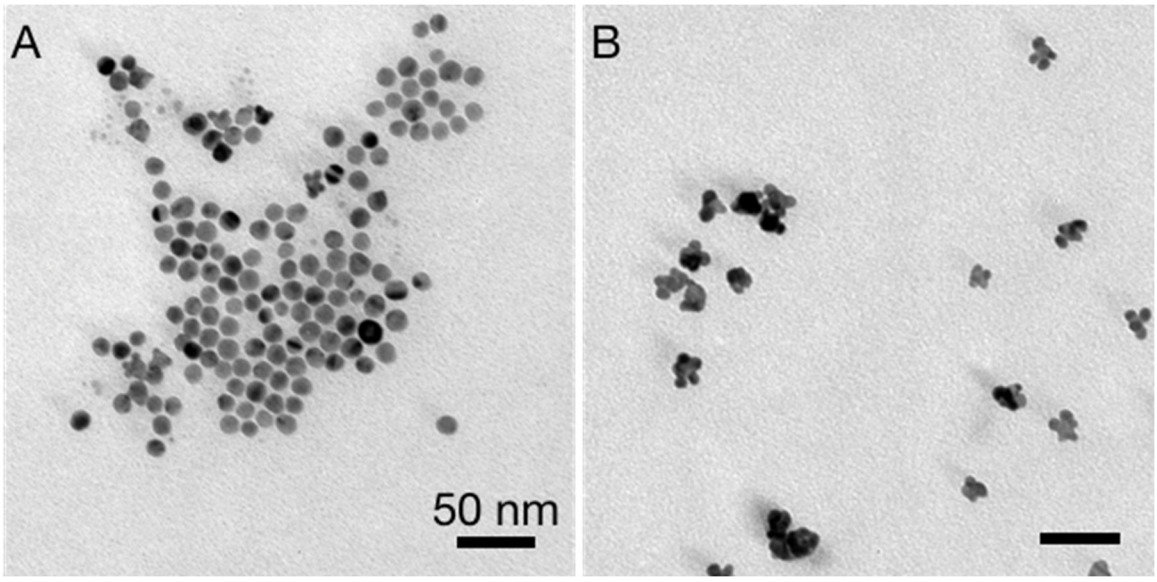

Figure S16. Low-magnification TEM images of galvanic replacement products obtained from adding (A) 4 and (B) 16 mL 0.1 mM $HAuCl_4$ to random alloy PdCu templates. (A) was taken from the same TEM sample as Figure S14B, and (B) from the same TEM sample as Figure S14D, many grid squares away from the images in Figure S14.

Discussion of A1 replacement product polydispersity. Where Figures S2, S3 and S4 showed mostly monodisperse samples with a relatively small window of polydisperse samples, Figure S16 suggests that polydisperse samples are common for random alloy templates. Figure S16 provides examples of images taken at different locations on the same TEM grids used for Figures S15B and S15D. Images of entire clusters of spheroids separated from clusters of dumbbell-like particles by distances of several TEM grid squares lends weight to the suggestion made earlier that segregation in a polydisperse sample may influence the erratic behavior of the Cu:Pd ratio in Figure 3.

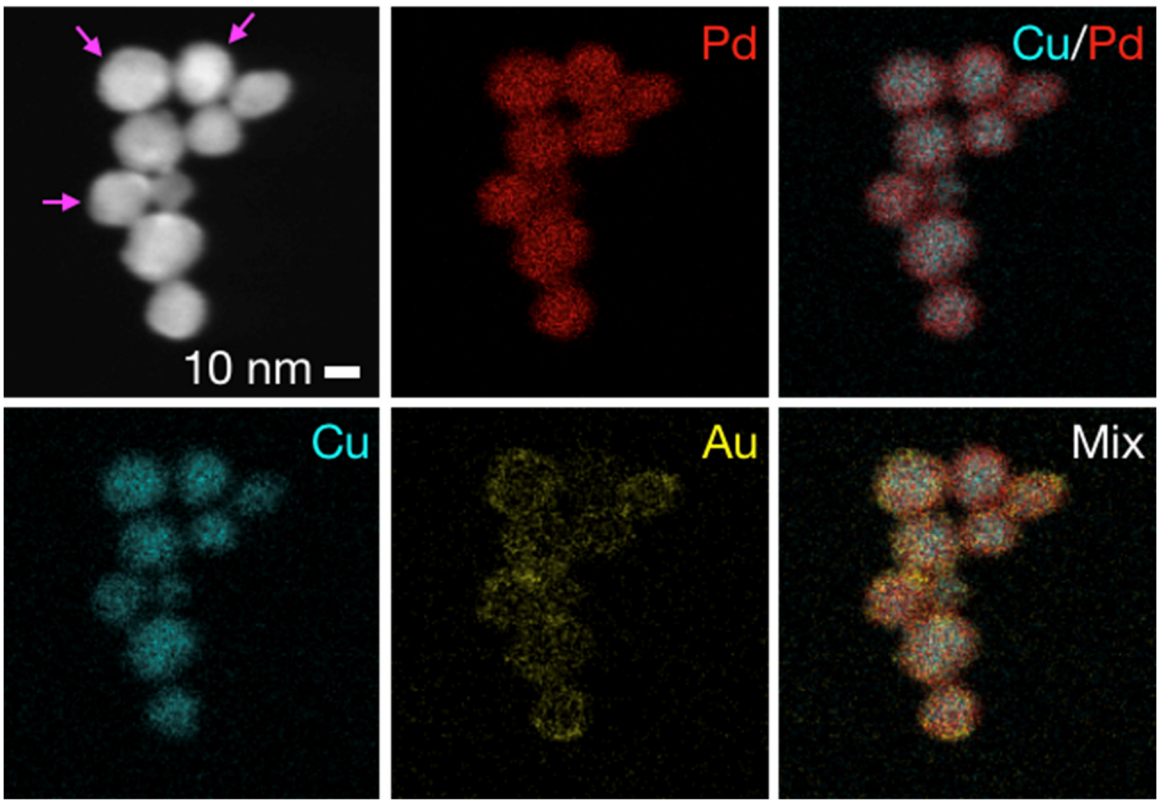

Figure S17. STEM image and corresponding EDS elemental map of galvanic replacement products obtained from adding 16 mL 0.1 mM $HAuCl_4$ to random alloy PdCu templates. Cyan, Cu; red, Pd; yellow, Au. Magenta arrows indicate particles at visibly different stages of replacement.

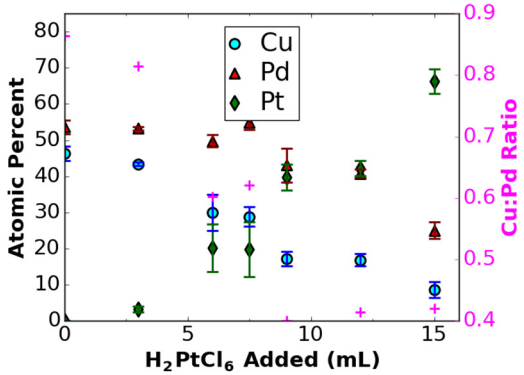

Figure S18. Evolving atomic percentages of Cu, Pd and Pt in intermetallic PdCu templates as 0.2 mM H_2PtCl_6 is added to them, as determined by energy dispersive X-ray spectroscopy. Error bars represent standard deviations.

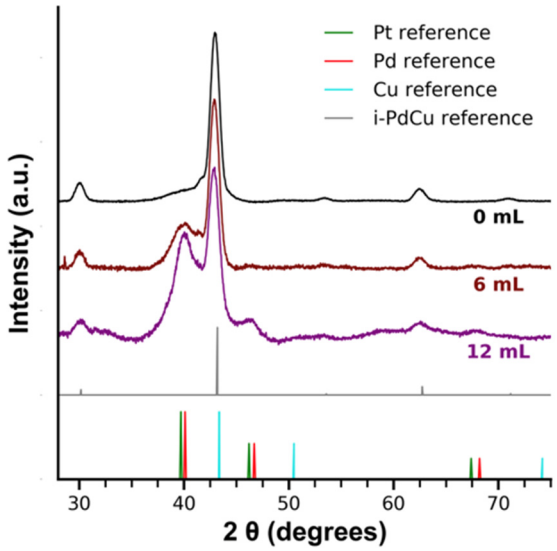

Figure S19. Background-subtracted XRD patterns corresponding to products obtained when intermetallic PdCu templates are galvanically replaced by various volumes of 0.2 mM H_2PtCl_6.

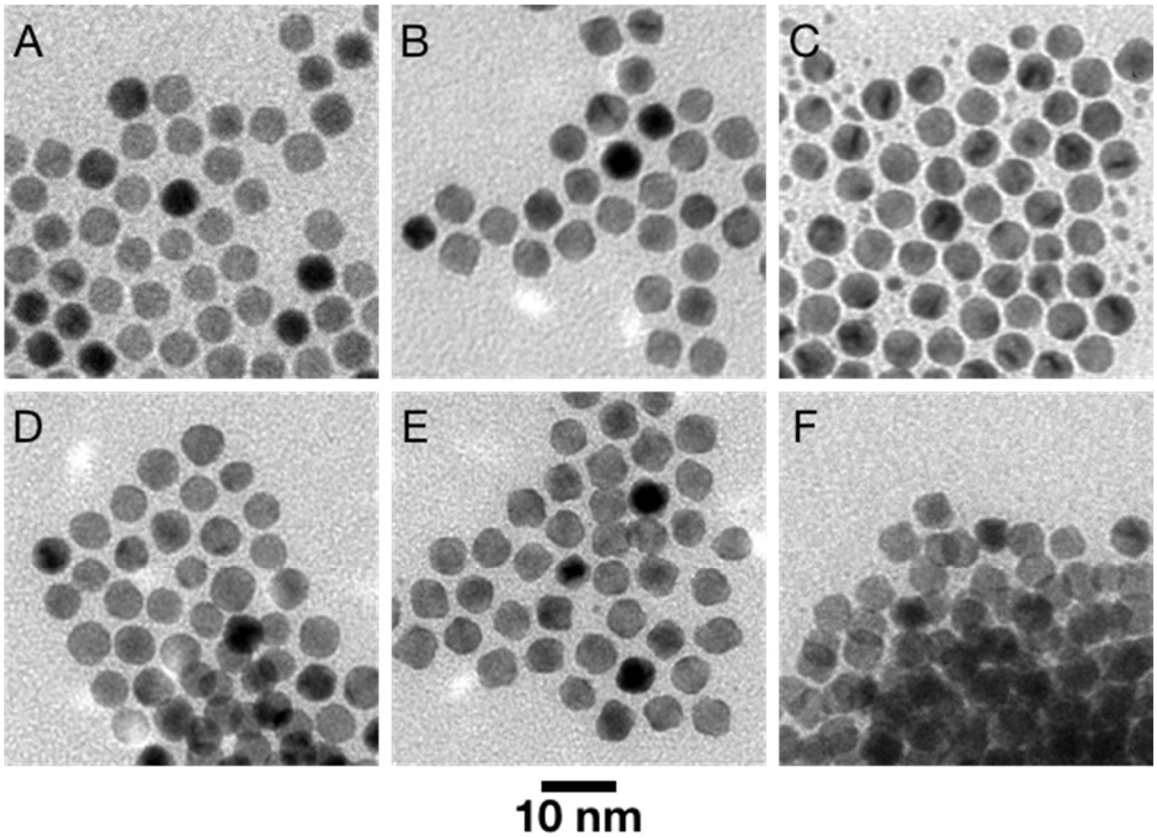

Figure S20. Low-magnification TEM images of galvanic replacement products obtained from adding (A) 3, (B) 4.5, (C) 6, (D) 7.5, (E) 9 and (F) 12 mL 0.2 mM H_2PtCl_6 to intermetallic PdCu templates.

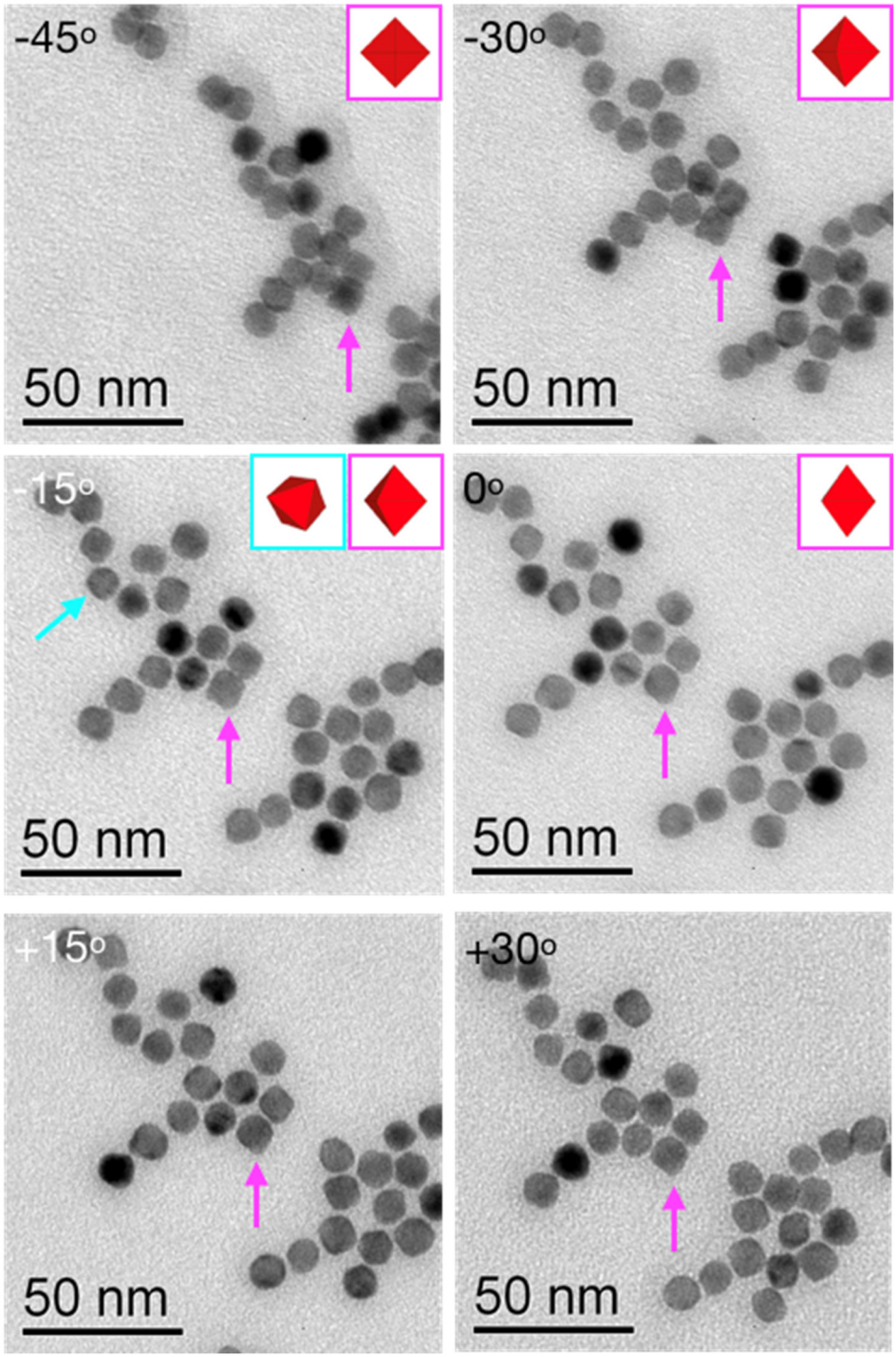

Figure S21. Low-magnification TEM images taken from multiple angles of a cluster of galvanic replacement products obtained from adding 6 mL 0.2 mM H_2PtCl_6 to intermetallic PdCu templates. Sample is tilted clockwise looking from the bottom of the image. Structural models correspond to particles tracked with cyan and magenta arrows

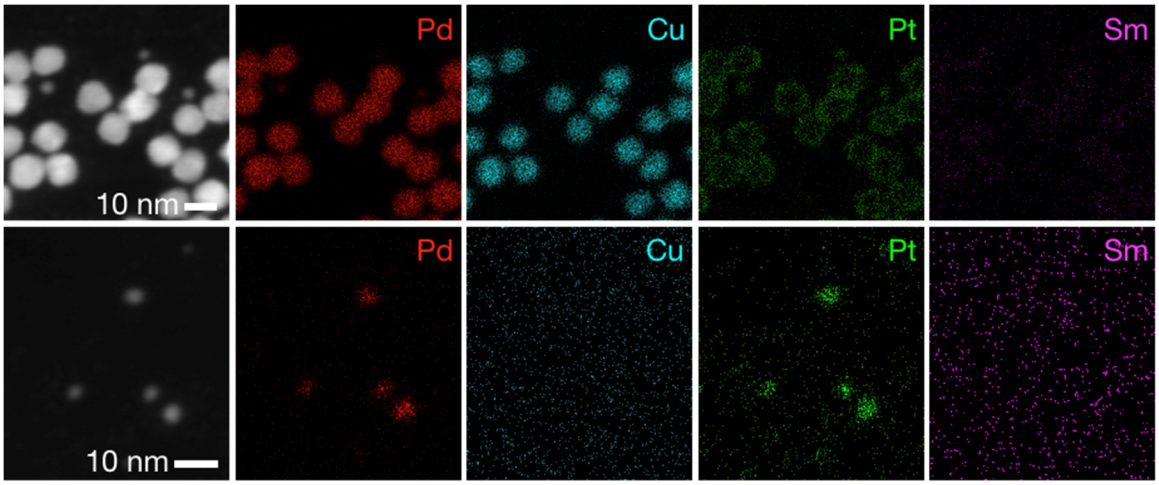

Figure S22. Lower-magnification STEM images and corresponding EDS elemental maps of two different spots on a sample obtained from adding 6 mL 0.2 mM H_2PtCl_6 to intermetallic PdCu templates. Cyan, Cu; red, Pd; green, Pt.

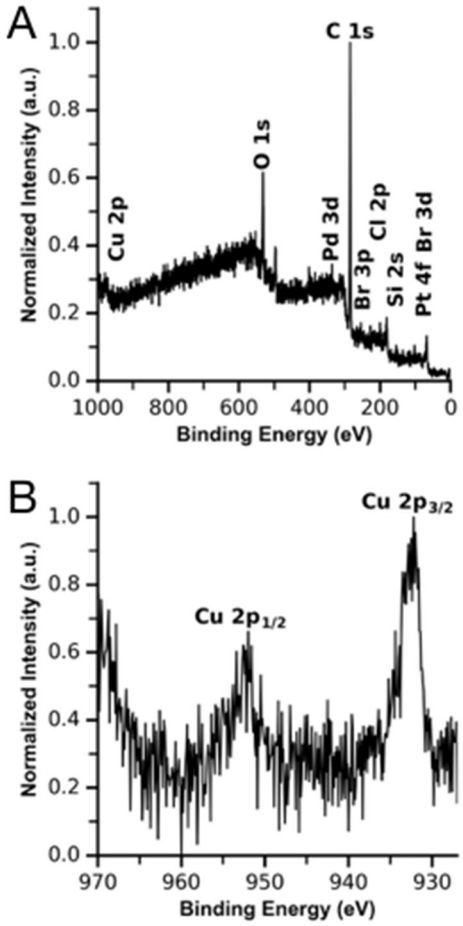

Figure S23. X-ray photoelectron spectra of the supernatant retrieved after centrifuging a galvanic replacement reaction solution in which 4.5 mL 0.2 mM H_2PtCl_6 were added to intermetallic PdCu templates, showing (A) survey scan and (B) high-resolution scan of Cu 2p region.

References

1. C. Wang, X. Sang, J. T. L. Gamler, D. P. Chen, R. R. Unocic and S. E. Skrabalak, *Nano Lett.*, 2017, **17**, 5526-5532.
2. J. T. L. Gamler, A. Leonardi, H. M. Ashberry, N. N. Daanen, Y. Losovyj, R. R. Unocic, M. Engel and S. E. Skrabalak, *ACS Nano*, 2019, **13**, 4008-4017.
3. L. Wu, J. Yu, L. Chen, D. Yang, S. Zhang, L. Han, M. Ban, L. He, Y. Xu and Q. Zhang, *J. Mater. Chem. C*, 2017, **5**, 3065-3071.
4. S. E. Skrabalak, L. Au, X. Li and Y. Xia, *Nat. Protoc.*, 2007, **2**, 2182-2190.
5. Lattice Constants of the elements, https://periodictable.com/Properties/A/LatticeConstants.an.html, (accessed October 27, 2020).
6. B. H. Toby and R. B. Von Dreele, *J. Appl. Crystallogr.*, 2013, **46**, 544-549.
7. C. de Mello Donega, P. Liljeroth and D. Vanmaekelbergh, *Small*, 2005, **1**, 1152-1162.
8. Y. Wang, H. C. Peng, J. Liu, C. Z. Huang and Y. Xia, *Nano Lett.*, 2015, **15**, 1445-1450.